

Synthesis and Application of MnO₂/PANI/MWCNT Ternary Nanocomposite as an Electrode Material for Supercapacitors

Yingying Huang¹, Jinlin Lu¹, Shumei Kang¹, Duo Weng¹, Lu Han², Yongfei Wang^{2,*}

¹ School of Materials and Metallurgy, University of Science and Technology Liaoning, Anshan 114051, China.

² School of High Temperature Materials and Magnesite Resources Engineering, University of Science and Technology Liaoning, Anshan 114051, China.

*E-mail: jvenile@163.com

Received: 18 March 2019 / Accepted: 28 July 2019 / Published: 5 August 2019

In this article, a ternary nanocomposite comprising MnO₂/PANI/MWCNTs was synthesized by a facile chemical method for application as an electrode material for supercapacitors. The morphology and microstructure of the nanocomposite were examined by using energy dispersive spectroscopy, X-ray diffraction, Fourier transform infrared spectrometry, field emission scanning electron microscopy and transmission electron microscopy. The electrochemical behavior of the ternary nanocomposite was investigated in a 1 M KOH aqueous solution by cyclic voltammetry, charge-discharge (CD) testing and electrochemical impedance spectroscopy. The ternary MnO₂/PANI/MWCNT nanocomposite demonstrated a specific capacitance of 395.0 F·g⁻¹ and can still maintain 72% of its capacitance after 1000 CD cycles at a current density of 1 A·g⁻¹. The excellent electrochemical properties of the MnO₂/PANI/MWCNT nanocomposite may arise from the high conductivity and the synergistic effect of the ternary structure.

Keywords: Supercapacitor, Multi-walled carbon nanotube, Polyaniline, Manganese dioxide, Electrochemical performance

1. INTRODUCTION

In recent years, environmental pollution and energy crises have ignited interest in developing renewable and sustainable energy sources [1-6]. Accordingly, developing high-performance energy storage devices is necessary owing to the instability of alternative energy resources, such as from the wind, sun and tides [7-9]. Among various energy storage/conversion devices, supercapacitors are becoming one of the most prominent energy storage systems due to their high and fast capability, long cycle life, wide operating range and low maintenance cost compared to batteries [10]. Therefore,

supercapacitors have been applied widely in hybrid electric vehicles, portable electronics, microautonomous robots and backup power systems [11, 12].

Supercapacitors have two types of charge storage mechanisms: electric double-layer capacitors (EDLCs) and redox supercapacitors. The charge storage mechanisms of EDLCs occur at or near the interface between the electrode and the electrolyte [13]. Some carbon materials are often used for electrode materials in EDLCs, such as carbon nanotubes (CNTs), graphene porous carbon and carbon onions [14-17]. Redox supercapacitors are also called pseudocapacitors, whose storage charges through reversible redox reactions. The reactions occur not only at the surface of the electrode but also near the surface of the solid electrode [8]. Transition metal oxides and conducting polymers are considered promising materials in pseudocapacitors. These materials often have specific advantages and disadvantages [18]. Transition metal oxides, such as manganese oxide (MnO_2) and ruthenium oxide (RuO_2), are usually used as active electrode materials due to their low cost, high energy density and specific energy capacity [19]. However, the problems of agglomeration, low operating voltage and poor cycle capability of the transition metal oxides have caused a major bottleneck in their performance and resulted in their limited application [20]. Conducting polymer materials are considered the most promising electrode materials in pseudocapacitors, such as polyaniline (PANI), polypyrrole and polythiophene, owing to their better redox properties and environmental friendliness [21, 22]. In particular, PANI has many advantages, such as a controllable morphology, relatively good electrical conductivity and simple fabrication process [23, 24]. However, PANI has poor cycling stability because of swelling and shrinkage during the charge and discharge processes [25, 26]. Recently, many researchers have explored various methods to fabricate binary and ternary composites with different functional materials for pseudocapacitors to solve the intrinsic problems [27-29]. For example, Guo et al. [30] synthesized a 3D porous CNT/ MnO_2 by a simple “dipping and drying” process followed by a potentiostatic deposition technology. Sivakkumar [31] developed a PANI/MWCNT composite by in situ chemical polymerization for supercapacitors. Shen et al. [34] developed a PANI/graphene/CNT composite with a good cycle performance of over 91% after 5000 cycles. These reports indicated that composite materials can enhance the electrochemical performance of supercapacitors.

In this work, we prepared a polyaniline/multiwalled carbon nanotube (PANI/MWCNT) nanocomposite using a facile strategy. The structure and electrochemical performance of the composites were characterized and studied in detail. The as-synthesized ternary MnO_2 /PANI/MWCNT nanocomposite shows much higher specific capacitance and better cyclic stability than the binary nanocomposite materials.

2. EXPERIMENTAL SECTION

2.1 Materials

Commercial multiwalled carbon nanotubes (MWCNTs, 30-50 nm in diameter, 5-15 μm in length, purity ≥ 95 wt%) were purchased from Shenzhen Nanotech Port Co., Ltd., potassium permanganate (KMnO_4), concentrated sulfuric acid (H_2SO_4), potassium hydroxide (KOH), aniline (ANI), ammonium persulfate (APS), acetylene black, polyvinylidene fluoride (PVDF), activated carbon and 1-methyl-2-

pyrrolidone were purchased from Shanghai Macklin Biochemical Co., Ltd. All reagents were A. R. grade and were used as received.

2.2 Synthesis of MnO_2 /MWCNT nanocomposite

The MnO_2 /MWCNT nanocomposite was synthesized as follows: 100 mg MWCNTs and 2.5 g $KMnO_4$ were dissolved in 100 mL deionized water. After stirring for 10 min, 0.5 mL concentrated H_2SO_4 was added into the above solution, and then the solution was stirred for 30 min at room temperature. The above slurry was transferred to a water bath at 80 °C and stirred for 1 h. Finally, the product was washed, filtered and vacuum-dried at 60 °C for 12 h.

2.3 Synthesis of PANI/MWCNTs and MnO_2 /PANI/MWCNT nanocomposite

PANI/MWCNT nanocomposites were synthesized by in situ chemical oxidation polymerization on the surface of the MWCNTs. The detailed steps were as follows: 200 mg MWCNTs was ultrasonically dispersed in 240 mL deionized water. Then, 1 mL of ANI and 3 g of APS were added into the above mixture. After that, the mixture was stirred at room temperature for 12 h. The slurry was washed with deionized water and ethanol. Finally, the precipitate was dried under vacuum at 60 °C for 24 h.



Figure 1. The fabrication procedure for the ternary nanocomposite MnO_2 /PANI/MWCNTs.

The fabrication procedure of MnO_2 /PANI/MWCNT nanocomposite is schematically presented in Figure 1. In short, 0.2 g PANI/MWCNT nanocomposite and 2.5 g $KMnO_4$ were dissolved in 200 mL deionized water, and then 0.5 mL H_2SO_4 was added into the solution. After that, the solution was stirred for 30 min. Finally, the sample was washed, filtered and vacuum-dried at 60 °C for 12 h.

2.4 Material characterization

X-ray diffraction (XRD) patterns were obtained by a PANANO X-ray diffractometer in the 2θ range of $10\text{-}90^\circ$ with Cu $K\alpha$ radiation ($\lambda = 0.154060$ nm). Fourier transform infrared (FTIR) spectra of the samples were conducted using an Agilent Technologies Cary 630 FTIR spectrometer at room temperature with a wavenumber range from 600 to 4000 cm^{-1} . The surface morphology, microstructure and energy dispersive spectroscopy (EDS) of the samples were investigated using field emission scanning electron microscopy (FESEM, ZEISS SIGMA) and transmission electron microscopy (TEM, HITACHI 600).

2.5 Preparation of working electrode and electrochemical measurement

The active materials, namely the MWCNTs and the PANI/MWCNT, $\text{MnO}_2/\text{MWCNT}$ and $\text{MnO}_2/\text{PANI}/\text{MWCNT}$ nanocomposites, were mixed with PVDF and acetylene black in a mass ratio of $80:10:10$. Then, the mixtures were dissolved in 1-methyl-2-pyrrolidone and stirred magnetically to form a homogeneous slurry. The slurry was coated on a nickel foam substrate with a size $1.5\text{ cm} \times 1.5\text{ cm}$. Finally, the coated nickel foams were dried at $60\text{ }^\circ\text{C}$ for 8 h in a vacuum oven. The active materials in each nickel foam electrode were controlled at approximately 4 mg.

The electrochemical properties of the working electrodes were conducted with a standard three-electrode system in $1.0\text{ M Na}_2\text{SO}_4$ aqueous solution as the electrolyte. The standard three-electrode testing system included a working electrode, a counter electrode (Pt foil) and a reference electrode (saturated calomel electrode, SCE). Cyclic voltammograms (CV), charge-discharge (CD) curves and electrochemical impedance spectroscopy (EIS) were measured by a CHI760E electrochemical workstation. The potential window of CV and CD ranged from $-0.4\text{~}0.4\text{ V}$. EIS was recorded at the frequency range of 0.01 to 10^5 Hz with open circuit potential. The cycle life was conducted on a LANHE CT2001A testing system by galvanostatic charge-discharge techniques. The specific capacitance can be calculated according to the following equation: $C_s = It/mV$, where C_s (F g^{-1}), I (A), t (s), m (g) and V (V) represent the specific capacitance, discharge current, discharge time, mass of active material and window potential, respectively [31].

3. RESULTS AND DISCUSSION

3.1 Chemical and structural analysis

The crystalline identity of the nanocomposite structures was confirmed by XRD and the patterns were displayed in Figure 2(a).

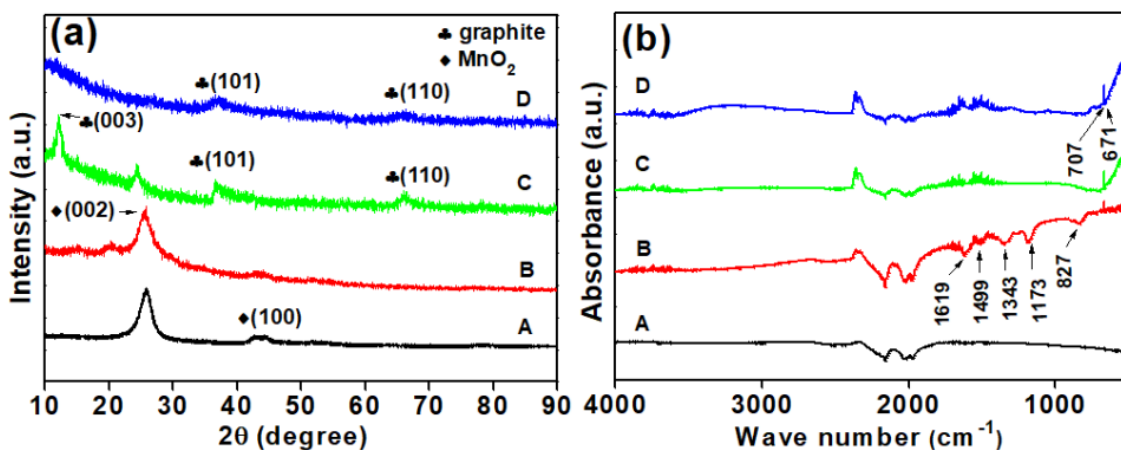


Figure 2. (a) XRD patterns and (b) FTIR results of (A): MWCNTs, (B): PANI/MWCNTs, (C): MnO₂/MWCNTs and (D): MnO₂/PANI/MWCNTs.

The diffraction patterns for the MWCNTs and PANI/MWCNT nanocomposite exhibit a peak at a 2θ value of 25.8° , which can be attributed to the basal plane (002) of graphite. In comparison with the MWCNTs and PANI/MWCNT nanocomposite, the (002) peak shifts to 23.6° for the MnO₂/MWCNT nanocomposite. The graphite diffraction peak at 43.1° corresponding to the (100) facet appears in the pattern for the MWCNTs. However, it disappeared in the pattern for the PANI/MWCNT nanocomposite and MnO₂/MWCNT nanocomposite. It is possible that PANI and MnO₂ formed on the surface of MWCNTs, resulting in a weak diffraction peak intensity for the graphite [33]. In the pattern for the MnO₂/MWCNT nanocomposite, the peaks at 2θ values of approximately 12.1° , 36.6° and 66.1° can be attributed to the (003), (101) and (110) reflections from polycrystalline orthorhombic MnO₂, respectively (JCPDS X-ray-diffraction standard card No. 00-030-0820). However, the MnO₂ peaks become broad in the MnO₂/PANI/MWCNT nanocomposite pattern, and it is possible that the presence of the PANI weakens the MnO₂ peak intensity [32]. This indicates that the MnO₂/PANI/MWCNT nanocomposite can be synthesized by a facile chemical process.

The FTIR spectra of the samples are shown in Figure 2(b). The MnO₂/MWCNT and MnO₂/PANI/MWCNT nanocomposites show absorbance bands at 671 cm^{-1} and 707 cm^{-1} , which are attributed to the stretching vibration and bending vibration of Mn-O groups in the MnO₂ crystals, respectively [27]. In the spectra of PANI/MWCNT and MnO₂/PANI/MWCNT nanocomposites, the peaks at 1619 cm^{-1} and 1499 cm^{-1} are attributed to the C=C stretching vibration of the quinoid ring and the benzenoid ring in the PANI chains, respectively [33]. The peaks at 1343 cm^{-1} , 1173 cm^{-1} and 827 cm^{-1} are attributed to the C-N stretching band, stretching of C=N (-N=quinoid=N-) and out of plane bending vibration of C-H in the benzene ring, respectively [34]. The intensities of the absorbance bands decrease in intensity after depositing MnO₂ on the surfaces of PANI/MWCNT nanocomposite.

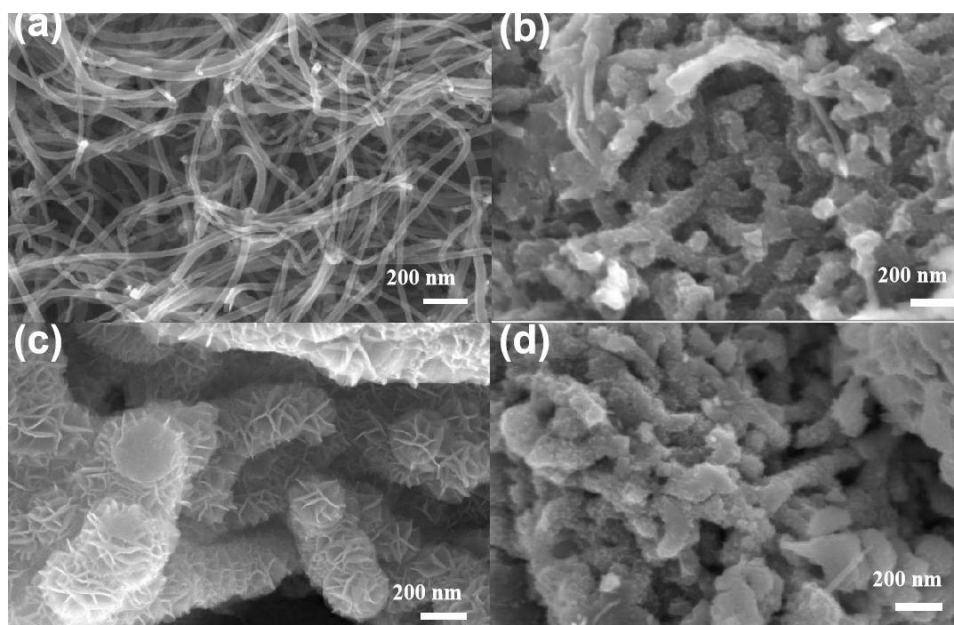


Figure 3. FESEM images of (a) MWCNTs, (b) PANI/MWCNTs, (c) MnO₂/MWCNTs and (d) MnO₂/PANI/MWCNTs.

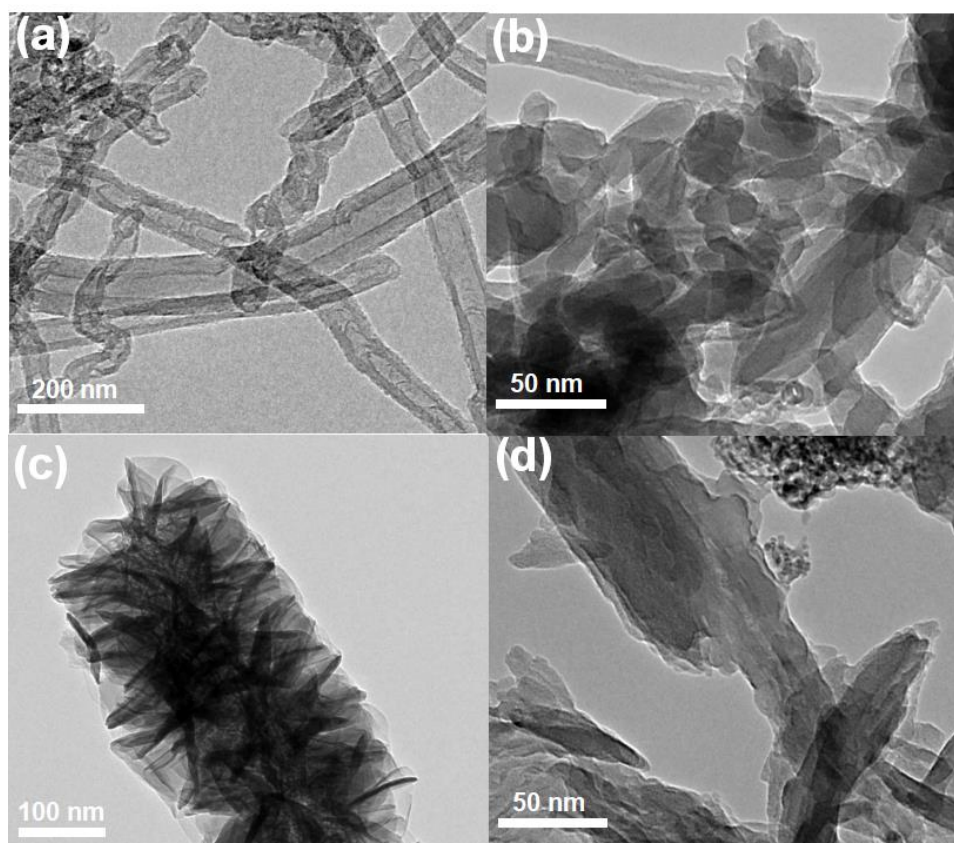


Figure 4. TEM images of (a) MWCNTs, (b) PANI/MWCNTs, (c) MnO₂/MWCNTs and (d) MnO₂/PANI/MWCNTs.

FESEM and TEM were used to characterize the structure and morphology of the nanocomposites, and the results are shown in Figure 3 and Figure 4, respectively. Figure 3(a) shows the SEM image of MWCNTs. The diameters of the MWCNTs are approximately 20~50 nm, and the lengths are tens of micrometers. When PANI was combined with the MWCNTs, many tiny protuberances can be seen on the surface of MWCNTs in Figure 3(b). Figure 3(c) displays MnO₂ with a whisker-like structure on the surface of the MWCNTs. In the case of the MnO₂/MWCNT nanocomposite, the average size of the particle is ~270 nm. Figure 3(d) shows the SEM images of MnO₂/PANI/MWCNT nanocomposite. The MnO₂/PANI/MWCNT nanocomposite becomes rougher than the PANI/MWCNT nanocomposite. It is possible that both the MnO₂ layer and nanowhisker MnO₂ grow on the surface of PANI/MWCNT nanocomposite [36, 37]. Figure 4(a) shows the TEM image of MWCNTs. It can be seen that the diameter of is ~30 nm. This result is in accordance with the FESEM image. Figure 4(b) shows the TEM image of PANI/MWCNT nanocomposite. Many nanoflakes can be clearly observed on the surface of MWCNTs. Figure 4(c) shows the TEM image of MnO₂/MWCNT nanocomposite. MnO₂ with a whisker-like structure adheres to the surface of the MWCNTs. The MnO₂/PANI/MWCNT nanocomposite displays a core-double-shell structure consisting of MWCNTs inside, PANI in the middle and MnO₂ on the outside, as shown in Figure 4(d).

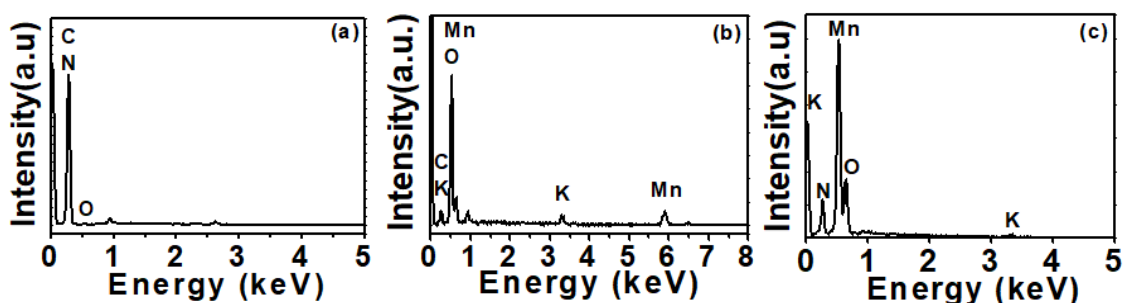


Figure 5. The EDS spectrum of (a) PANI/MWCNTs, (b) MnO₂/MWCNTs and (c) MnO₂/PANI/MWCNTs.

Figures 5(a), 5(b) and 5(c) show the EDS results for the PANI/MWCNT, MnO₂/MWCNT and MnO₂/PANI/MWCNT nanocomposites, respectively. C, O and N are contained in the PANI/MWCNT nanocomposite. Mn, O and C are contained in the MnO₂/MWCNT nanocomposite. Mn, C, O and N are contained in the MnO₂/PANI/MWCNT nanocomposite. The results indicate that binary and ternary nanocomposites have been successfully synthesized by the facile chemical synthesis process.

3.2 Electrochemical Properties

The electrochemical properties of the MWCNTs and the PANI/MWCNT, MnO₂/MWCNT and MnO₂/PANI/MWCNT nanocomposites were investigated by different electrochemical testing techniques with a three-electrode system in a 1 M KOH aqueous solution. Figure 6 shows the EIS measurement results of MWCNT, PANI/MWCNT, MnO₂/MWCNT and MnO₂/PANI/MWCNT electrodes. The frequency ranges from 10⁵ Hz to 0.01 Hz at the open-circuit potential.

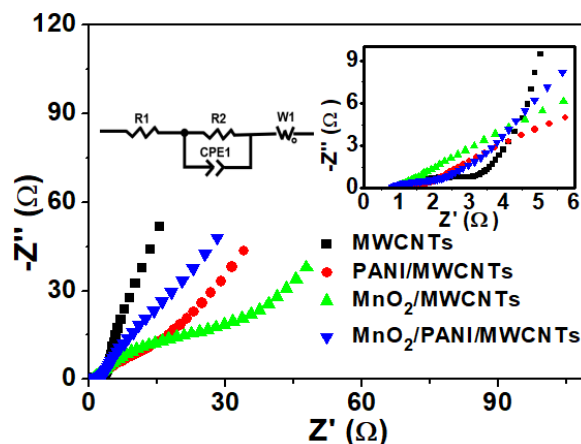


Figure 6. Nyquist plots of the electrode materials in the frequency range of 10^5 Hz to 0.01 Hz.

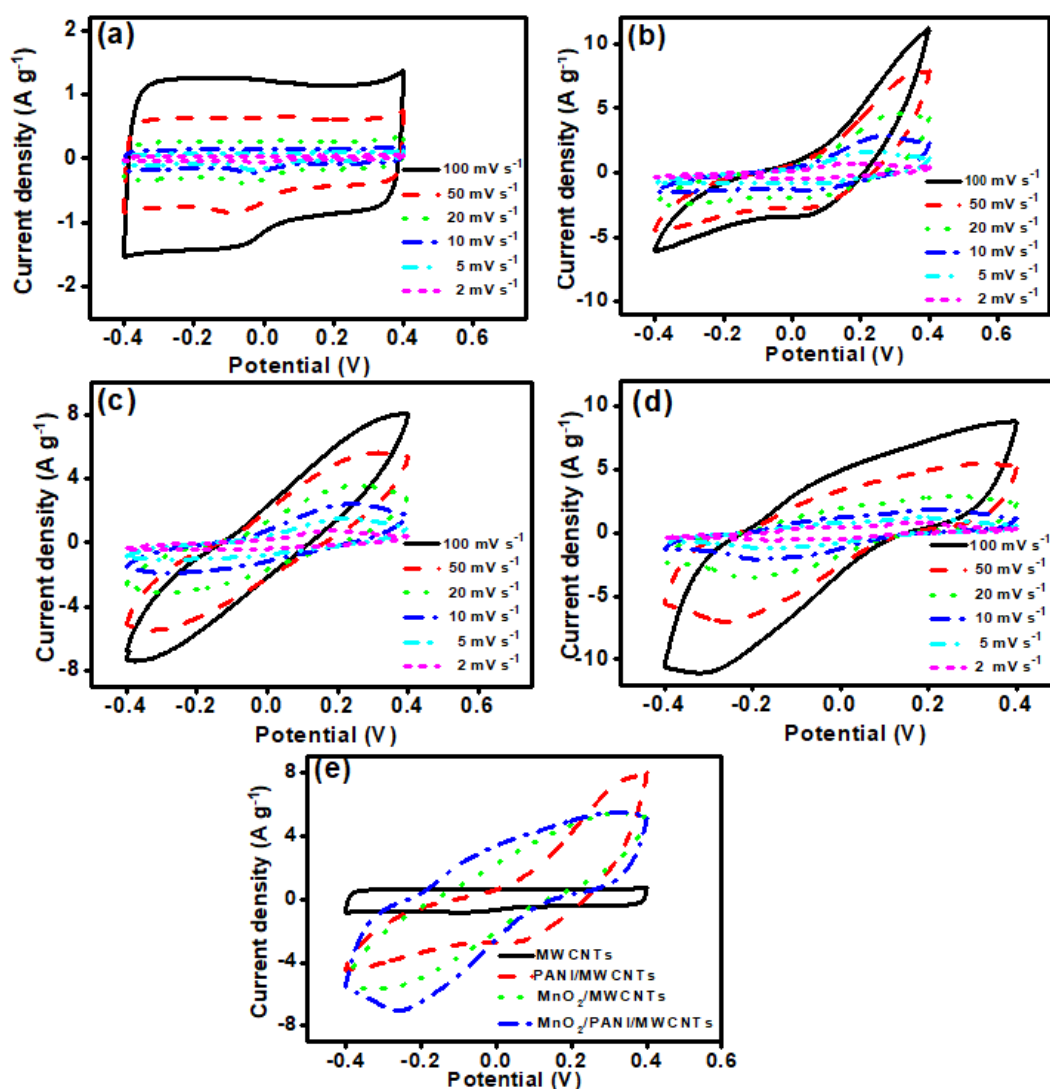


Figure 7. CV curves of (a) MWCNTs, (b) PANI/MWCNTs, (c) MnO_2 /MWCNTs, (d) MnO_2 /PANI/MWCNTs and (e) CV curves of the different electrode materials at a scan rate of $50 \text{ mV} \cdot \text{s}^{-1}$ in 1.0 M KOH solution.

The EIS spectra of the electrodes can be divided into two regions: the high-frequency arc region and the low-frequency line region. The spectrum on the real axis (Z') represents the equivalent series resistance (ESR), which includes the ionic resistance of the electrolyte, the intrinsic resistance of the active material and current collector, and the contact resistance at the interface of the electrode and electrolyte [38-40]. The ESR values are 1.07 Ω , 0.94 Ω , 0.90 Ω and 0.82 Ω for the MWCNT, PANI/MWCNT, MnO₂/MWCNT and MnO₂/PANI/MWCNT electrodes, respectively. The high-frequency region of the spectrum corresponds to the charge transfer resistance (R_{ct}), and the R_{ct} values are estimated to be 1.9 Ω , 1.4 Ω , 34.7 Ω and 1.8 Ω for the MWCNT, PANI/MWCNT, MnO₂/MWCNT and MnO₂/PANI/MWCNT electrodes, respectively [41, 42]. The inset of Figure 5 is the equivalent circuit mode.

The CV curves for the MWCNTs and the PANI/MWCNT, MnO₂/MWCNT and MnO₂/PANI/MWCNT nanocomposites are shown in Figure 7(a-d) with different scan rates from 2 mV s⁻¹ to 100 mV·s⁻¹ in a potential window of -0.4 to 0.4 V. Figure 7(a) shows the CV curves of MWCNTs. The CV curves exhibit good rectangular and symmetric shapes, suggesting fast reversible Faradic reactions and ideal capacitive behavior [43]. The CV curves of the MnO₂/MWCNT, PANI/MWCNT and MnO₂/PANI/MWCNTs nanocomposites are shown in Figure 7(b), 7(c) and 7(d), respectively. The shape of the CV curves does not change below 20 mV·s⁻¹, and the peak current density increases as the scan rate increases. This indicates that they have good rate properties and excellent capacitance behavior [44]. The CV curves gradually lost their rectangular shape with increasing scan rate. Figure 7(e) shows the CV curves for the MWCNTs and the PANI/MWCNT, MnO₂/MWCNT and MnO₂/PANI/MWCNTs nanocomposites at a scan rate of 50 mV·s⁻¹. The CV curve of the MnO₂/PANI/MWCNT nanocomposite has the largest area, indicating that the MnO₂/PANI/MWCNT electrode has the highest specific capacitance. This may be caused by the synergistic effect and the special structure of the nanocomposites [45].

Figure 8(a-d) shows the CD curves for the MWCNTs and the PANI/MWCNT, MnO₂/MWCNT and MnO₂/PANI/MWCNT electrodes at different current densities from 1 to 5 A·g⁻¹ in the potential range between -0.4 and 0.4 V. All the curves exhibit nearly linear responses, implying that the electrodes have supercapacitive characteristics [46]. In addition, a small amount of voltage decrease (IR drop) can be seen from the curves, indicating that the electrodes have a low internal resistance, which is very important for the supercapacitor electrodes [47]. Figure 8(e) shows the CD curves for the MWCNTs and the PANI/MWCNT, MnO₂/MWCNT and MnO₂/PANI/MWCNT electrodes at a current density of 1 A·g⁻¹. The specific capacitances of the MWCNTs and the PANI/MWCNT, MnO₂/MWCNT and MnO₂/PANI/MWCNT electrodes were calculated to be 20.25 F·g⁻¹, 170 F·g⁻¹, 241.25 F·g⁻¹ and 395 F·g⁻¹, respectively.

The MnO₂/PANI/MWCNT electrode has the largest specific capacitance. Figure 8(f) shows a function for the specific capacitance of the MWCNTs and the PANI/MWCNT, MnO₂/MWCNT and MnO₂/PANI/MWCNT electrodes at different current densities.

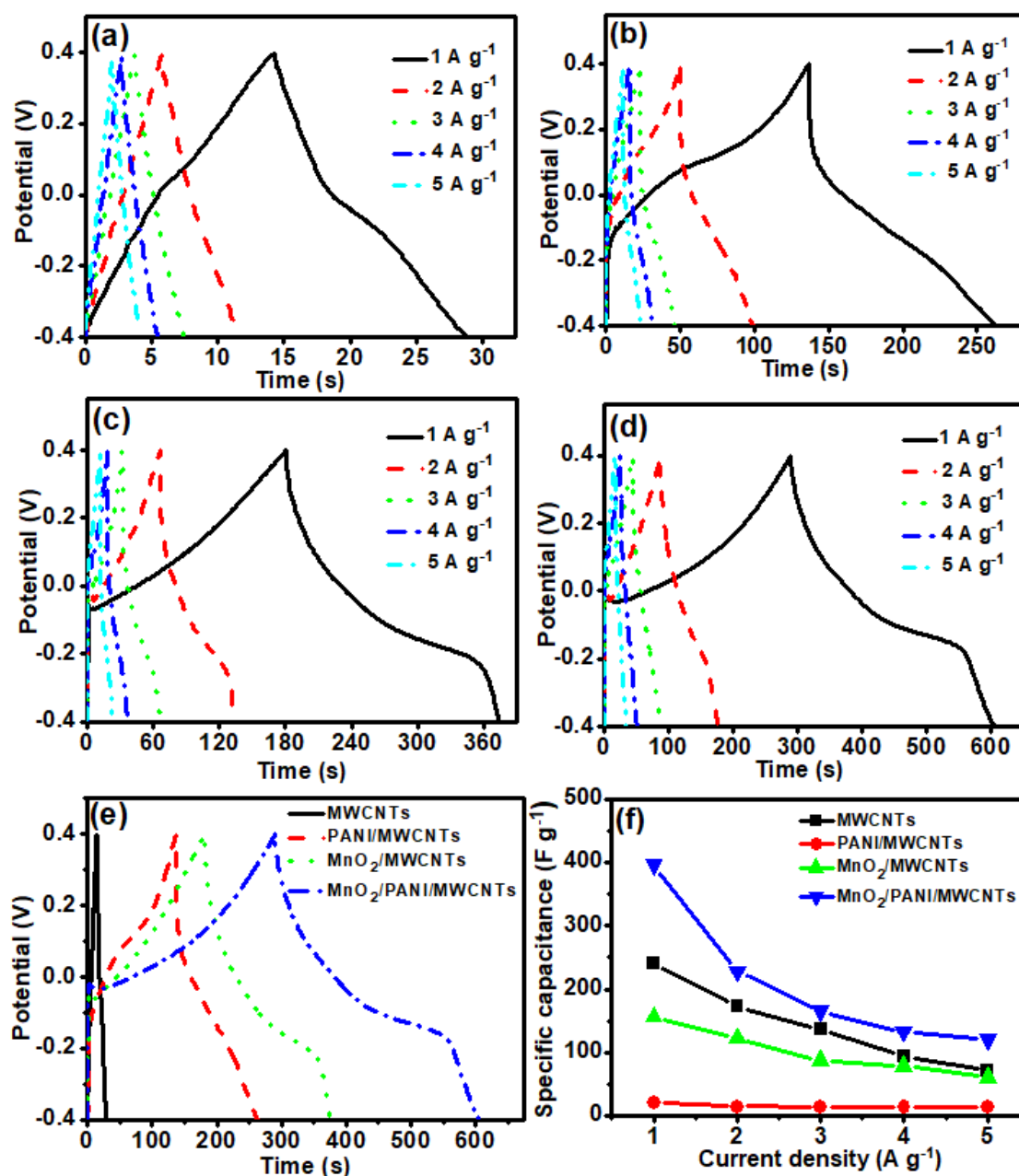


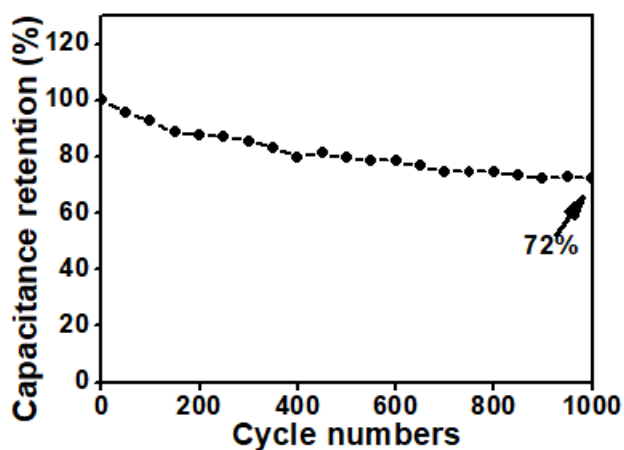
Figure 8. CD curves of (a) MWCNTs, (b) PANI/MWCNTs, (c) MnO₂/MWCNTs, (d) MnO₂/PANI/MWCNTs, (e) CD curves of the electrode materials at a current density of 1 A·g⁻¹ in 1.0 M KOH and (f) Specific capacitance of the electrode materials at different current densities.

The specific capacitance decreases with increasing current density, and the MnO₂/PANI/MWCNT electrode delivers the largest capacitance at all current densities. The excellent properties can be ascribed to MnO₂ and PANI grown on the surface of MWCNTs, which can increase the contact area between the ions and electrolyte. Meanwhile, the porous structure of the MWCNTs is beneficial for fast ion adsorption-desorption and reversible redox reactions [48]. In addition, the specific capacitance of MnO₂/PANI/MWCNT electrode is higher than those reported previously (see Table 1) when considering the same current density.

Table 1. Comparison of the specific capacitance of current work and relevant reports.

Ref.	Samples	Specific capacitance ($F g^{-1}$)
49	Polyaniline-deposited porous carbon	180 ($0.3 mV s^{-1}$)
50	CNT/polypyrrole/ MnO_2	149 ($1.0 mA cm^{-2}$)
51	CNT/ MnO_2	160.5 ($1 A g^{-1}$)
52	Graphene/ MnO_2 /polyaniline	276 $F g^{-1}$
53	Graphene/polyaniline composite paper	233 ($2 mV s^{-1}$)
54	Polyaniline grafed reduced graphe oxide	250 ($100 mV s^{-1}$)
55	Modified graphene/polyaniline nanocomposites	242 ($1.5 A g^{-1}$)
56	Graphene/polyaniline nanofibers composite paper	301 ($0.5 A g^{-1}$)
57	Amide group-connected graphene polyaniline nanofiberhybrid	369 ($1 A g^{-1}$)
Current work	MnO_2 /PANI/MWCNTs	395 $F g^{-1}$

Cyclic lifetime is an important factor for supercapacitor applications. The cyclic stability of the MnO_2 /PANI/MWCNT electrode was measured at a current density of $1 A \cdot g^{-1}$ for 1000 cycles, and the result is shown in Figure 9. After 1000 CD cycles, the MnO_2 /PANI/MWCNT electrode exhibited a specific capacitance retention of 72%, indicating good stability of the electrode for long cycle life.

**Figure 9.** Cycling performances of the MnO_2 /PANI/MWCNTs at the current density of $1 A \cdot g^{-1}$ (1000 charge and discharge cycles).

4. CONCLUSION

In summary, PANI/MWCNT, MnO_2 /MWCNT and MnO_2 /PANI/MWCNT nanocomposites were synthesized by a facile chemical process. The as-prepared ternary MnO_2 /PANI/MWCNT electrode showed the highest specific capacitance value of $395 F \cdot g^{-1}$ and a long cycle life of 72% of its initial capacitance after 1000 CD cycles. The significant enhancement of electrochemical performance is attributed to the ternary structure and synergistic effect from each component of PANI, MnO_2 and the conductive MWCNT network. The MWCNT network can not only reduce the internal resistance of the

ternary but also maintain the structural stability. These results indicate that the MnO₂/PANI/MWCNT nanocomposite is promising as an electrode material for application in supercapacitors.

ACKNOWLEDGEMENTS

This work was supported by the National Natural Science Foundation of China (51774177, 51504133), Natural Science Foundation Guidance Program of Liaoning Province (20170540468, 20170540465), Liaoning Bai Qian Wan Talents Program (2017-104), Program of Distinguished Professor of Liaoning Province (2017-60), Project of Department of Education of Liaoning Province (2017LNQN14, 2016TSZD06), Innovative Research Team Funding of USTL (No. 2016TD05)

References

1. L.L. Zhang, X.S. Zhao, *Chem. Soc. Rev.*, 38 (2009) 2520-2531.
2. L. Dai, D.W. Chang, J.B. Baek, W. Lu, *Small*, 8 (2012) 1130-1166.
3. Y. He, W. Chen, C. Gao, J. Zhou, X. Li, E. Xie, *Nanoscale*, 5 (2013) 8799-8820.
4. T. Bordjiba, M. Mohamedi, L.H. Dao, *Advanced Materials*, 20 (2010) 815-819.
5. B. Liu, P. Soares, C. Checkles, Y. Zhao, G. Yu, *Nano Letters*, 13 (2013) 3414-3419.
6. G. Yu, X. Xie, L. Pan, Z. Bao, Y. Cui, *Nano Energy*, 2 (2013) 213-234.
7. B.E. Conway, Plenum Press, 1999.
8. J.R. Miller, P. Simon, *Science*, 321 (2008) 651-652.
9. L. Wu, J. Zheng, L. Wang et al. *Angewandte Chemie International Edition*, (2018).
10. A.G. Pandolfo, A.F. Hollenkamp, *Journal of Power Sources*, 157 (2006) 11-27.
11. Y. Huang, J. Liang, Y. Chen, *Small*, 8 (2012) 1805-1834.
12. P. Tang, L. Han, L. Zhang, *Acs Appl Mater Interfaces*, 6 (2014) 10506-10515.
13. B. Deore, Plenum Press, 1999.
14. L. Mao, K. Zhang, H.S.O. Chan, J. Wu, *Journal of Materials Chemistry*, 22 (2012) 1845-1851.
15. G. Yu, L. Hu, N. Liu, H. Wang, M. Vosgueritchian, Y. Yang, Y. Cui, Z. Bao, *Nano Letters*, 11 (2015) 4438.
16. J. Chen, S.A. Ashraf, G.G. Wallace, A.I. Minett, P.A. Folkes, P. Sherrell, D. Antiohos, P. Aitchison, A.T. Harris, *Journal of Materials Chemistry*, 21 (2011) 15987-15994.
17. Y. Zhao, J. Liu, Y. Hu, H. Cheng, C. Hu, C. Jiang, L. Jiang, A. Cao, L. Qu, *Advanced Materials*, 25 (2013) 591-595.
18. M. Beidaghi, Y. Gogotsi, *Energy & Environmental Science*, 7 (2014) 867-884.
19. S.W. Lee, B.M. Gallant, H.R. Byon, P.T. Hammond, S.H. Yang, *Energy & Environmental Science*, 4 (2011) 1972-1985.
20. M. Liu, W.W. Tjiu, J. Pan, C. Zhang, W. Gao, T. Liu, *Nanoscale*, 6 (2014) 4233-4242.
21. S.I. Cho, S.B. Lee, *Accounts of Chemical Research*, 2008, 41(6):699-707.
22. Y.R. Lin, H. Teng, *Carbon*, 41 (2003) 2865-2871.
23. G. Fabian, Y. Zi-You, W. Jin-Long, Y. Shu-Hong, L. Yong, *Small*, 11 (2015) 4666-4672.
24. L. Dong, G. Liang, C. Xu, W. Liu, Z.Z. Pan, E. Zhou, F. Kang, Q.H. Yang, *Nano Energy*, 34 (2017) 242-248.
25. Z. Yin, H. Zhou, C. Fu, N. Zhang, Y. Kuang, *Rsc Advances*, 6 (2016) 41142-41150.
26. L. Mingkai, M. Yue-E, Z. Chao, T.W. Weei, Y. Zhibin, P. Huisheng, L. Tianxi, *Nanoscale*, 5 (2013) 7312-7320.
27. Y. Huang, D. Weng, L. Han, Y. Wang, K. Liu, J. Yan, J. Lu, *Nanoscience & Nanotechnology Letters*, (2017).
28. H. Xia, Y. Wang, J. Lin, L. Lu, *Nanoscale Research Letters*, 7 (2012) 33.
29. B.J. Lee, SIVAKKUMAR, R. S., K.O. JANG MYOUN, J.H. Kim, J.O. SEONG MU, Y.K. Dong, *Journal of Power Sources*, 168 (2007) 546-552.

30. C. Guo, L. Hua, Z. Xuan, H. Huo, C. Xu, *Sensors & Actuators B Chemical*, 206 (2015) 407-414.
31. S.R. Sivakkumar, J.K. Wan, J.A. Choi, D.R. Macfarlane, M. Forsyth, D.W. Kim, *Journal of Power Sources*, 171 (2007) 1062-1068.
32. H. Fan, H. Wang, N. Zhao, X. Zhang, J. Xu, *Journal of Materials Chemistry*, 22 (2012) 2774-2780.
33. T.M. Wu, Y.W. Lin, *Polymer*, 47 (2006) 3576-3582.
34. K. Zhang, L.L. Zhang, X.S. Zhao, J. Wu, *Chemistry of Materials*, 22 (2010) 1392-1401.
35. V. Gupta, N. Miura, *Materials Letters*, 60 (2006) 1466-1469.
36. J.G. Wang, Y. Yang, Z.H. Huang, F. Kang, *Journal of Materials Chemistry*, 22 (2012) 16943-16949.
37. Q. Li, J. Liu, J. Zou, A. Chunder, Y. Chen, Z. Lei, *Journal of Power Sources*, 196 (2011) 565-572.
38. J. Gamby, P.L. Taberna, P. Simon, J.F. Fauvarque, M. Chesneau, *Journal of Power Sources*, 101 (2001) 109-116.
39. Maowen Xu, Lingbin Kong, A. Wenjia Zhou, Hulin Li, *Journal of Physical Chemistry C*, 112 (2007).
40. X.Y. Cao, X. Xing, N. Zhang, H. Gao, M.Y. Zhang, Y.C. Shang, X.T. Zhang, *Journal of Materials Chemistry A*, 3 (2015) 3785-3793.
41. Q. Yang, X.T. Zhang, M.Y. Zhang, Y. Gao, H. Gao, X.C. Liu, H. Liu, K.W. Wong, W.M. Lau, *Journal of Power Sources*, 272 (2014) 654-660.
42. S. Hassan, M. Suzuki, S. Mori, A.A. Elmoneim, *Rsc Advances*, 4 (2014) 20479-20488.
43. L. P, Y. Y, S. E, S. Q, S. Y, W. S, W. J, W. K, Z. H, Y. Q, C. A, W. D, *Acs Applied Materials & Interfaces*, 6 (2014) 5228-5234.
44. J. Yan, T. Wei, B. Shao, Z. Fan, W. Qian, M. Zhang, F. Wei, *Carbon*, 48 (2010) 487-493.
45. A.K. Sharma, Y. Sharma, R. Malhotra, J.K. Sharma, *Advanced Materials Letters*, 3 (2012).
46. Q. Zhang, L. Li, Y. Wang, Y. Chen, F. He, S. Gai, P. Yang, *Electrochimica Acta*, 176 (2015) 542-547.
47. A.L.M. Reddy, M.M. Shaijumon, S.R. Gowda, P.M. Ajayan, *Journal of Physical Chemistry C*, 117 (2010) 658-663.
48. A.K. Das, R. Bera, A. Maitra, S.K. Karan, S. Paria, L. Halder, S.K. Si, A. Bera, B.B. Khatua, *Journal of Materials Chemistry A*, 5 (2017).
49. W. C. Chen, T. C. Wen and H. S. Teng, *Electrochim. Acta*, 48 (2003) 641-649.
50. S R Sivakkumar, J M Ko, D Y Kim, *Electrochimica Acta*, 2007, 52(25) 7377-7385.
51. C. Y. Guo, H. Li, X. Zhang, H. H. Huo, C. L. Xu, *Sensors and Actuators B: Chemical*, 206 (2015) 407-414.
52. G. Wang, Q. Tang, H. Bao, *Journal of Power Sources*, 241 (2013) 231-238.
53. N. A. Kumar, H. J. Choi, Y. R. Shin, *Acs Nano*, 6 (2012) 1715-23.
54. D. W. Wang, F. Li, J. Zhao, *Acs Nano*, 3 (2009) 1745-1752.
55. S. Sahoo, G. Karthikeyan, G. C. Nayak, Das, C. K. *Macromol, Res.*, 20 (2012) 415-421.
56. S. Liu, X. H. Liu, Z. P. Li, S. G. Yang, J. Q. Wang, *New J. Chem.*, 35 (2011) 369-374.
57. J. H. Liu, J. W. An, Y. C. Zhou, Y. X. Ma, M. L. Li, M. Yu, S. M. Li, *ACS Appl. Mater. Interfaces* 4 (2012) 2870-2876.